

HyperPotter: Spell the Charm of High-Order Interactions in Audio Deepfake Detection

Qing Wen¹, Haohao Li¹, Zhongjie Ba^{*1,2}, Peng Cheng^{*1,2}, Miao He¹, Li Lu^{1,2}, Kui Ren^{1,2,3}

¹The State Key Laboratory of Blockchain and Data Security, Zhejiang University

²Hangzhou High-Tech Zone (Binjiang) Institute of Blockchain and Data Security

³Shanghai Institute for Advanced Study, Zhejiang University

February 6, 2026

Abstract

Advances in AIGC technologies have enabled the synthesis of highly realistic audio deepfakes capable of deceiving human auditory perception. Although numerous audio deepfake detection (ADD) methods have been developed, most rely on local temporal/spectral features or pairwise relations, overlooking high-order interactions (HOIs). HOIs capture discriminative patterns that emerge from multiple feature components beyond their individual contributions. We propose HyperPotter, a hypergraph-based framework that explicitly models these synergistic HOIs through clustering-based hyperedges with class-aware prototype initialization. Extensive experiments demonstrate that HyperPotter surpasses its baseline by an average relative gain of 22.15% across 11 datasets and outperforms state-of-the-art methods by 13.96% on 4 challenging cross-domain datasets, demonstrating superior generalization to diverse attacks and speakers.

1 Introduction

The emergence of AIGC enables highly realistic synthetic speech, supporting legitimate applications such as audiobooks while introducing serious security risks [1]. Recent reports indicate a surge in illicit activities using AI-generated voices [2]. In particular, voice forgery has been utilized to spread misinformation, commit identity fraud, and influence political campaigns [3, 4]. As speech synthesis quality improves, artifacts distinguishing real and synthetic speech become increasingly subtle and distributed across multiple acoustic dimensions, posing challenges for effective detection.

To distinguish synthetic from authentic audio, extensive efforts have been devoted to audio deepfake detection (ADD). Existing ADD approaches rely on CNN-, graph-, or Transformer-based architectures to learn discriminative artifacts [5, 6, 7]. Despite their effectiveness, most approaches predominantly rely on **local or pairwise interactions** as basic relational units. For instance, convolutional operators focus on localized patterns, attention mechanisms compute pairwise token affinities, and graph-based models aggregate information along binary edges, limiting their ability to characterize joint behavior across multiple embeddings.

In complex systems, interactions involving more than two elements may exhibit behaviors that cannot always be reduced to pairwise dependencies, known as **high-order interactions (HOIs)** [8]. In speech signals, synthetic artifacts often arise from complementary manipulations across temporal dynamics, spectral structures, and latent feature representations, such that discriminative patterns may only emerge when multiple features are considered jointly. Capturing these collective behaviors therefore requires modeling HOIs. However, such HOIs remain unexplored in existing ADD works.

To characterize these collective behaviors in speech synthetic artifacts, we adopt O-information [9], a theoretical measure that distinguishes whether HOIs convey predominantly **synergistic** or **redundant** information. As illustrated in Figure 1 (left), synergy captures information that is only available when multiple elements are considered jointly, whereas redundancy reflects information duplicated across them. In the context of ADD, we hypothesize that *high-order synergistic interactions play a critical role in capturing generalizable*

* Corresponding authors: zhongjieba@zju.edu.cn; peng_cheng@zju.edu.cn

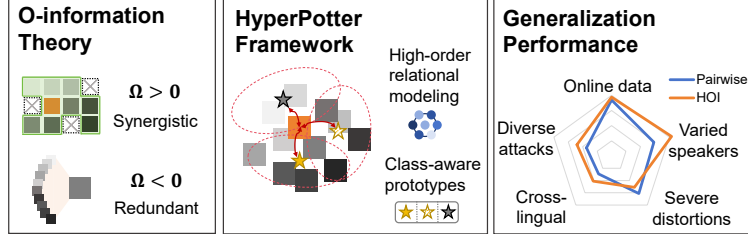


Figure 1: Motivated by O-information analysis, the HyperPotter framework enables high-order relation modeling and achieves competitive generalization performance across diverse scenarios.

synthetic artifacts. To empirically support this hypothesis, we evaluate a representative high-order synergistic relational modeling tool across multiple scenarios (Figure 1 right*).

To instantiate such high-order modeling, we propose a prototype-oriented hypergraph detection framework, namely **HyperPotter**. Unlike pairwise graphs that may redundantly encode similar evidence across edges, hypergraphs represent multi-way dependencies as unified hyperedges, offering a natural structure for modeling synergistic HOIs. HyperPotter incorporates two key components: 1) a relational artifact amplification module that emphasizes informative synergistic artifacts, and 2) a class-aware prototype-oriented hyperedge initialization mechanism for efficient relational construction. Our contributions are summarized as follows:

1. We provide the first investigation of high-order effects in audio deepfake detection from an information-theoretic perspective, revealing the importance of synergistic interactions beyond pairwise dependencies.
2. We propose HyperPotter, a novel hypergraph-based detection framework that explicitly models high-order synergistic relations via prototype-guided hyperedge construction and relational artifact enhancement.
3. Extensive experiments on 13 diverse datasets demonstrate that HyperPotter consistently improves cross-scenario generalization under diverse spoofing algorithms and speaker conditions, highlighting the practical benefits of modeling high-order synergy.

Overall, this work underscores the importance of high-order interactions in audio deepfake detection and demonstrates that explicitly modeling synergistic dependencies offers an effective path toward improved generalization.

2 Related Works

2.1 Audio Deepfake Detection

Early works used GMM [10] classifiers to process handcrafted features, such as MFCC, LFCC [11], and CQCC [12]. With the development of deep learning, end-to-end models have become prevalent. For instance, RawNet2 [5] constructs residual CNNs to capture the subtle details. RawGAT-ST [13] and AASIST [6] transform waveforms into temporal-spectral heterogeneous graphs. Self-supervised learning (SSL) front-ends [14], usually comprising CNNs and Transformers, have leveraged large-scale speech knowledge to enhance detection robustness [7, 15, 16]. However, these works primarily focus on local or pairwise relationships, overlooking the complex HOIs in heterogeneous artifacts.

2.2 Hypergraph

Hypergraph neural networks [17] have been widely used to model high-order relations in recommendation [18], time series forecasting [19], and LLM enhancement [20]. They are also effective in capturing complex multimodal dependencies. In computer vision, ViHGNN [21] models correlations among image patches, and the subsequent works further improve performance through multi-scale hyperedges [22] or virtual vertices [23]. In the audio domain, LHGNN [24] achieves good performance in audio classification by combining local and high-order relations. However, we have not seen the exploration of hypergraph for ADD despite the importance of relational representation in this domain.

*The comparison is supported by the statistics in Table 6.

2.3 Prototype Mechanism

Prototype learning has been extensively studied for unsupervised domain adaptation, where class prototypes provide stable class-aware representations that address sampling variability and class imbalance [25] and are used to assign pseudo-labels [26]. Recent advances extend this mechanism to anomaly detection via intrinsic normal prototypes extracted from test images [27] and incremental deepfake detection using prototype similarity for replay selection [28]. We leverage class-aware prototypes to initialize hyperedges, constructing semantically meaningful groupings that capture high-order interactions in audio features.

3 Analysis for HOIs in ADD

Existing literature lacks a theoretical analysis of leveraging HOIs in ADD. In this section, we employ the O-information theory proposed by Rosas *et al.* [9] to characterize HOI effects in the context of the ADD task. We first introduce key concepts to understand how HOIs behave differently in redundancy- versus synergy-dominated systems. In redundancy-dominated systems, HOIs can be decomposed into combinations of pairwise relations; however, in synergy-dominated systems, pairwise relations cannot fully capture HOIs. This fundamental gap motivates us to explore high-order structures beyond pairwise networks and compare two different modeling strategies for ADD.

3.1 Information-theoretic Descriptions of HOIs

Let $\mathbf{X}^n = (X_1, \dots, X_n)$ denote the set of n random variables representing the feature space in ADD (e.g., multi-view representations). The uncertainty of the system is measured by the Shannon entropy $H(\mathbf{X}^n)$. The sum of the entropies for each individual variable is $\sum_{i=1}^n H(X_i)$, which is not less than $H(\mathbf{X}^n)$.

Following the description by Rosas *et al.*, HOIs are modeled as the multivariate interdependencies in the system. To quantify the interdependencies, we utilize two complementary metrics. First, *total correlation* or *multi-information* measures the degree of information redundancy among variables, defined as the sum of individual entropies minus the joint entropy:

$$C(\mathbf{X}^n) := \sum_{i=1}^n H(X_i) - H(\mathbf{X}^n),$$

High $C(\mathbf{X}^n)$ indicates that the variables are statistically correlated, imposing collective constraints on the system. On the other hand, *dual total correlation* or *binding information* quantifies the shared information bound within the group, which cannot be reduced to individual contributions:

$$B(\mathbf{X}^n) := H(\mathbf{X}^n) - \sum_{i=1}^n H(X_i | \mathbf{X}_{-i}^n),$$

where $\mathbf{X}_{-i}^n = (X_1, \dots, X_{i-1}, X_{i+1}, \dots, X_n)$. And the sum of $H(X_i | \mathbf{X}_{-i}^n)$ quantifies individual private randomness that cannot be inferred from observing other variables. Thus, $B(\mathbf{X}^n)$ reflects the synergistic information rooted in the high-order structure.

The *O-information* unifies these two metrics to determine the dominant nature of the multivariate interdependency:

$$\begin{aligned} \Omega(\mathbf{X}^n) &:= C(\mathbf{X}^n) - B(\mathbf{X}^n) \\ &= (n-2)H(\mathbf{X}^n) + \sum_{i=1}^n [H(X_i) - H(\mathbf{X}_{-i}^n)]. \end{aligned}$$

The sign of $\Omega(\mathbf{X}^n)$ serves as a quantitative indicator: $\Omega(\mathbf{X}^n) > 0$ indicates a **redundancy-dominated** system ($C > B$). The same information is duplicated across multiple feature channels under a large set of constraints, providing robustness but low uniqueness. $\Omega(\mathbf{X}^n) < 0$ indicates a **synergy-dominated** state ($B > C$). The system depends on strong high-order constraints where information is emergent, effectively capturing synthesis artifacts that are invisible in isolation but evident when features are jointly analyzed.

3.2 A New Perspective Beyond Pairwise Interactions in ADD

In the context of an ADD system, the observable variables are audio embeddings extracted from a waveform sample. When most embeddings encode similar artifacts ($\Omega(\mathbf{X}^n) > 0$), identification results remain largely unchanged whether one considers individual embeddings or the entire embedding set. In contrast, when embeddings exhibit high randomness and diversity ($\Omega(\mathbf{X}^n) < 0$), reliable identification can only be achieved by modeling the synergistic structure of their interdependencies, instead of focusing on isolated parts.

Armed with the *O-information* framework, we analyze the underpinnings of current ADD approaches. Pairwise relations (i.e., edges in standard graphs) are primarily suited to modeling redundancy-dominated interactions ($\Omega(\mathbf{X}^n) > 0$), where information is relatively repetitive across node pairs. Consequently, mainstream ADD methods, which mainly rely on pairwise mechanisms (e.g., Transformer or AASIST), tend to implicitly assume that deepfake artifacts can be sufficiently characterized through redundant feature correlations.

However, this assumption is challenged by empirical observations in recent literature. First, information bottleneck analyses suggest that removing task-irrelevant redundancy (corresponding to an increase in $B(\mathbf{X}^n)$) facilitates the extraction of fundamental acoustic features to improve detection performance [29]. Second, it has been demonstrated that modeling interactions across disjoint frequency bands and temporal scales in heterogeneous networks leads to strong empirical performance [6]. These observations can be interpreted as capturing the weak (i.e., the low correlations between features) but key constraints related to $C(\mathbf{X}^n)$.

Although a rigorous quantification of the synergy in ADD remains an open problem, these observations motivate a paradigm shift. We hypothesize that *advanced deepfake artifacts contain a fair amount of synergy information*. Therefore, we propose to transition from redundancy-oriented pairwise models to a synergy-dominated system. To achieve this, we introduce hypergraphs, which naturally capture high-order relationships in systems characterized by highly nonlinear interactions [30], as the core architecture for our method. This paradigm shift could open a new route for understanding deepfake artifacts, thereby improving detection generalization.

4 Hypergraph-based Detection Framework

4.1 Overview

HyperPotter formulates the ADD task as a graph-level classification problem and is built around a memory-enhanced hypergraph attention layer (HAGNN), as illustrated in Figure 2. The input waveforms are first processed by an encoding network to derive node features for hypergraph construction. For each graph, HAGNN constructs FCM-based hyperedges capturing HOI patterns, which are then strengthened by an attention-driven relational artifact amplification module. These hyperedges are initialized under the guidance of prototypes introduced in the next section.

4.2 Node Feature Encoding

To transform raw waveforms into node-level representations, we adopt the graph construction module from Wav2Vec2-AASIST, further described in Appendix A. Specifically, the input waveforms are encoded by the pretrained XLS-R model together with a RawNet2 encoder. The encoded embeddings are aggregated along spectral and temporal dimensions to form two sets of nodes. These node representations serve as inputs to subsequent HAGNN layers.

Notation. We now introduce the notation for node representations from the encoding process. Let \mathcal{X} denote a batch of B audio samples. For an audio sample $b \in \{1, \dots, B\}$, we view its audio embeddings as a set of nodes and represent the sample as a hypergraph. Specifically, each sample is characterized by a node feature matrix $\mathbf{X}_b = [\mathbf{x}_{b,1}, \dots, \mathbf{x}_{b,N}]^\top \in \mathbb{R}^{N \times D}$, where N and D represent the number of nodes and the feature dimension. The hypergraph contains K hyperedges, where each hyperedge connects all nodes, resulting in a degree-free hypergraph with hyperedge degree \mathcal{D} . Each hypergraph is associated with a graph-level label $y_b \in \{0, 1\}$, consistent with the ground-truth label of the corresponding audio sample.

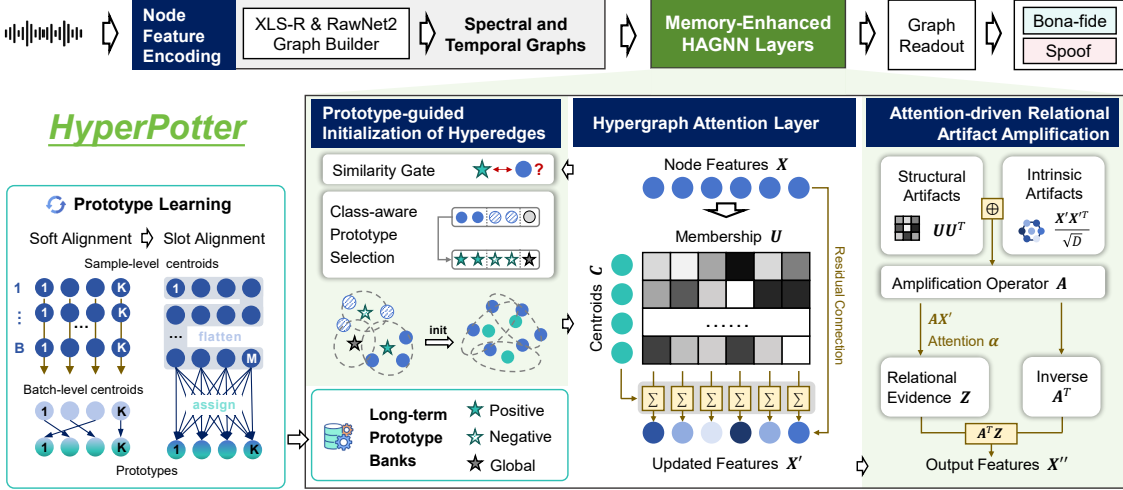


Figure 2: Overview of the HyperPotter framework. HyperPotter integrates hypergraph attention layers with prototype-guided hyperedge initialization to capture and amplify high-order relational artifacts, enabling effective aggregation of discriminative cues for generalizable audio spoofing detection.

4.3 Hypergraph Attention Layer

The HAGNN models latent relational patterns by leveraging hypergraph-based message passing [31]. It first aggregates node features into hyperedge representations via a FCM-based node-to-hyperedge mapping, and then propagates the resulting high-order relational information back to nodes through hyperedge-to-node message passing, thereby refining node representations.

Hyperedge Construction. A hyperedge is defined as a non-empty cluster of nodes that jointly characterize high-order relations [32]. Here, hyperedges are constructed through the Fuzzy C-Means (FCM) clustering method, which enables flexible modeling of node-hyperedge associations. Unlike hard clustering algorithms such as K-Means, FCM adopts a soft clustering strategy that allows each node to participate in multiple clusters to varying degrees. The soft clustering property makes FCM appropriate for modeling continuous associations in multimodal data [22, 24].

The FCM algorithm computes node feature distances to construct K overlapping clusters, namely hyperedges. FCM optimizes the node-cluster assignments through an iterative process that alternately updates centroids and membership values. Each cluster is centered around a single centroid. Further, the membership matrix $\mathbf{U} \in \mathbb{R}^{N \times K}$ is defined as a soft incidence matrix, where each node can participate in multiple hyperedges with different strengths.

For a given graph sample, the node features are denoted by $\mathbf{X} = [\mathbf{x}_1, \dots, \mathbf{x}_N]^\top$, where $\mathbf{x}_i \in \mathbb{R}^D$ represents the D -dimensional feature vector of the i -th node. For K hyperedges, their cluster centroids are $\mathbf{C} \in \mathbb{R}^{K \times D}$. The membership degree of node \mathbf{x}_i belonging to k -th hyperedge is represented by u_{ik} , where $0 \leq u_{ik} \leq 1$ and $\sum_{k=1}^K u_{ik} = 1$.

First, the membership matrix $\mathbf{U} \in \mathbb{R}^{N \times K}$ is initialized randomly. Then, the k -th centroid is computed as the membership-weighted average of node feature vectors:

$$\mathbf{c}_k = \frac{\sum_{i=1}^N (u_{ik})^m \mathbf{x}_i}{\sum_{i=1}^N (u_{ik})^m}, \quad (1)$$

where $m > 1$ is the fuzzifier parameter that controls the smoothness of U . When $m = 1$, FCM degenerates to the K-Means algorithm. Given updated centroids, the membership values are recomputed by:

$$u_{ij} = \frac{1}{\sum_{k=1}^K \left(\frac{d_{ij}}{d_{ik}} \right)^{\frac{2}{m-1}}}, \quad d_{ik} = \|\mathbf{x}_i - \mathbf{c}_k\| + \varepsilon, \quad (2)$$

where d_{ik} denotes the distance between node feature vector \mathbf{x}_i and centroid \mathbf{c}_k and ε is a small constant. A smaller distance d_{ij} results in a larger membership value u_{ij} .

The iterative update process terminates, indicating that hyperedge representations have stabilized, when either the maximum number of iterations is reached or the loss function converges. The standard FCM objective function is: $J(\mathbf{U}, \mathbf{C}) = \sum_{i=1}^N \sum_{k=1}^K u_{ik}^m \|\mathbf{x}_i - \mathbf{c}_k\|^2$.

Clustering Information Aggregation. Following the node-to-hyperedge clustering, the hyperedge-level representations are propagated back to nodes. Specifically, the hyperedge-to-node aggregation process updates node features via a residual fusion mechanism: $\mathbf{x}'_i = \beta_1 \mathbf{x}_i + (1 - \beta_1) \sum_{k=1}^K u_{ik} \mathbf{c}_k$, where β_1 balances the contribution of original features and the aggregated information from hyperedges.

4.4 Relational Artifact Amplification

Artifact Amplification Operator. To adapt the model for deepfake detection, we propose an operator designed to amplify the relational artifacts within the hypergraph and node embeddings. The relational representations are materialized by computing the self-similarity of structures and features. Specifically, structural artifacts are $\mathbf{A}^{(c)} = \mathbf{U}\mathbf{U}^\top$, while intrinsic feature-level artifacts are defined as: $\mathbf{A}^{(f)} = \frac{\mathbf{X}'\mathbf{X}^{\top}}{\sqrt{D}}$. The final operator, which fuses these two components, is formulated as $\mathbf{A} = \text{softmax}(\beta_2 \mathbf{A}^{(c)} + (1 - \beta_2) \mathbf{A}^{(f)})$, where β_2 is a balancing factor. Under this formulation, the connectivity between two nodes is amplified if they exhibit both similar structural consistency and feature-level agreement.

Attention-driven Amplification. Based on the operator A , we further introduce an attention mechanism to model manipulation traces. The node embeddings are transformed by the operator to extract relational evidence, denoted as $\mathbf{Z} = \mathbf{A}\mathbf{X}'$. An attention factor $\alpha = \text{softmax}(\mathbf{Z}\mathbf{w}_\alpha)$ is computed, where \mathbf{w}_α is a learnable weight vector. Finally, the relational evidence is integrated via a residual connection and projected back into the node space: $\mathbf{X}'' = \mathbf{A}^\top((1 + \alpha) \odot \mathbf{Z})$. This mechanism encourages the model to focus on the most informative relational artifacts.

5 Prototype Bank Design

While the previous section details the hypergraph construction and the feature amplification, effective feature aggregation depends heavily on high-quality initialization. As illustrated in the left panel of Figure 2, we introduce the "Prototype-guided Initialization" for FCM clustering, enabling hypergraph layers the capability of long-term memorization. The prototype bank module stores multiclass centroids for the FCM initialization process to speed convergence and improve detection performance.

5.1 Motivation

Problems of Randomly Initialized Hyperedges. The default initialization method of the FCM-based hyperedge generates the membership matrix randomly. Specifically, each batch constructs HOIs from scratch, which strongly affects the efficiency and quality of relationship construction.

Prototypes as Cross-batch Structural Priors. To facilitate hyperedge initialization, we incorporate historical structural knowledge through a long-term storage mechanism. Inspired by the semantic graph search scheme [33], we compress information from hypergraph centroids into prototypes, which serve as semantic anchors. Compared to vector databases [34] or anchor graphs [35], prototypes offer advantages in capturing global high-order concepts and enhancing computational efficiency. Furthermore, these prototypes are updated via a non-differentiable Exponential Moving Average (EMA), which significantly improves optimization stability.

5.2 Prototype-Guided Hyperedge Initialization

Components of a Prototype Bank. To better capture artifact characteristics, we maintain a prototype bank that captures both class-aware discriminative features and global structural information. Formally, the bank is defined as

$$\mathcal{P} = [\mathbf{P}^{(+)}, \mathbf{P}^{(-)}, \mathbf{P}^{(g)}]$$

, where each set $\mathbf{P} = \{\mathbf{p}_k\}_{k=1}^K$ contains K centroid-sized prototypes $\mathbf{p}_k \in \mathbb{R}^D$. Specifically, the class-conditional sets $\mathbf{P}^{(+)}$ and $\mathbf{P}^{(-)}$ leverage binary supervision to guide the clustering process, while the global set $\mathbf{P}^{(g)}$ serves as an alignment anchor to ensure overall feature consistency.

Prototype-guided Hyperedge Initialization Process. The process includes three sequential steps to refine the starting state of the FCM clustering:

1. **Similarity gating.** To restrict domain matching to established prototypes, a similarity controller first evaluates each batch. The similarity score s is defined as the cosine similarity between the batch-averaged features and the mean global prototypes: $s = \cos(\frac{1}{BN} \sum_{b=1}^B \sum_{n=1}^N \mathbf{x}_{b,n}, \frac{1}{K} \sum_{k=1}^K \mathbf{p}_k^{(g)})$. Batches with $s < \tau$, where τ is a predefined threshold, are filtered out to ensure feature alignment.
2. **Prototype selection.** We then adaptively select prototypes based on label availability, which varies between stages. Evaluation: Initialization centroids are directly inherited from $\mathbf{P}^{(g)}$. Training: We employ a class-aware initialization strategy to construct K centroids. The first 20% of the K slots are occupied by $\mathbf{P}^{(g)}$ to keep structural stability. The remaining slots are filled by randomly sampling $\mathbf{P}^{(+)}$ and $\mathbf{P}^{(-)}$, proportional to the ratio of bona-fide to spoof samples within the batch.
3. **External centroid injection.** The externally constructed centroids, augmented with a minor perturbation, are then injected into the FCM algorithm. These centroids define the initial node membership, which triggers the subsequent FCM optimization loops.

5.3 Prototype Learning Pipeline

We introduce a dynamic update mechanism that integrates batch knowledge into the prototype bank. This process extracts class-aware and global centroids from the batch, aligns these local centroids with historical prototypes, and performs an EMA-based integration.

Label-aware Centroids Estimation. To integrate supervised information, we perform an additional FCM iteration that updates class-aware batch centroids with membership values weighted by node labels. For brevity, we describe the formulation using positive prototypes as the representative case. For b -th sample, the class-conditional membership between n -th node and k -th cluster is $w_{b,nk}^{(+)} = (y_b \cdot u_{b,nk})^m$, where m is the fuzziness. Following the equation 1, this k -th positive centroid for this sample is computed as:

$$\hat{\mathbf{c}}_{b,k}^{(+)} = \frac{\sum_{n=1}^N w_{b,nk}^{(+)} \mathbf{x}_{b,n}}{\sum_{n=1}^N w_{b,nk}^{(+)} + \varepsilon}. \quad (3)$$

Semi-alignment Strategy. Since local clusters from the current batch may be misaligned with the features of global prototype banks, we adopt a progressive two-stage alignment strategy: a soft-alignment phase for batch-level consistency in early epochs, and a slot-alignment phase for precise feature aggregation (ensuring the precision and generalization of prototypes).

Soft Alignment facilitates the aggregation of irregular clusters in a batch. We compute batch-level centroids first, then update prototypes. Specifically, while the global batch centroid $\hat{\mathbf{c}}_k^{(g)}$ is the mean of all batch centroids, the class-aware batch centroids $\hat{\mathbf{c}}_k^{(+)}$ incorporates sample-level contributions. For class-aware batch centroids, we first determine the contribution of each sample for cluster k by define a weight as $\alpha_{b,k}^{(+)} = \sum_{n=1}^N w_{b,nk}^{(+)}$. The k -th global and positive batch centroids are updated as follows:

$$\hat{\mathbf{c}}_k^{(g)} = \frac{1}{B} \sum_{b=1}^B \mathbf{c}_{b,k}, \quad \hat{\mathbf{c}}_k^{(+)} = \frac{\sum_{b=1}^B \alpha_{b,k}^{(+)} \hat{\mathbf{c}}_{b,k}^{(+)}}{\sum_{b=1}^B \alpha_{b,k}^{(+)} + \varepsilon}. \quad (4)$$

Then the soft alignment strategy aligns the batch-level centroids with long-term prototypes. We employ a greedy matching algorithm based on cosine similarity to find the optimal centroid-prototype mapping π : $\pi = \text{argmax} \sum_{k=1}^K \cos(\mathbf{p}_k^{(g)}, \hat{\mathbf{c}}_{\pi(k)}^{(g)})$. After applying the permutation, the reordered centroids are given by $\tilde{\mathbf{c}}_k^{(g)} = \hat{\mathbf{c}}_{\pi(k)}^{(g)}$. The same permutation is used for both positive and negative centroids.

Table 1: EERs (%) comparison for different models trained on ASVspoof2019 LA. Lower is better. **Bold**, underline, and \dagger indicate the best, second-best, and third-best results, respectively. The subscripts indicate the performance gaps between HyperPotter and its baseline.

Model	Params (M)	In-the-Wild	ASV20 19LA	ASV20 21LA	ASV20 21DF	ASV spoof5	For	Codecfake	ADD22 Track1	ADD22 Track3	ADD23 R1	ADD23 R2	Libri Voc	SONAR
Wave2Vec2+AASIST [15]	317.84	11.19	0.221	0.82	6.63	16.24	7.46	43.36	<u>31.04</u>	16.52	27.74	21.92	11.13	46.12
XLSR+Conformer [16]	302.40	-	0.97	2.58	-	-	-	-	-	-	-	-	-	-
XLSR+Conformer+TCM [36]	319	7.79	0.19 \dagger	3.00	2.15	18.85	10.69	36.01	37.40	20.94	23.43	22.74	2.35	26.57 \dagger
XLSR+AASIST2 [37]	-	-	0.15	1.61	2.77	-	-	-	-	-	-	-	-	-
WaveLM+MFA [38]	-	-	0.42	5.08	2.56	-	-	-	-	-	-	-	-	-
XLSR+SLS [39]	340	7.45 \dagger	0.231	2.86	1.91	18.76	5.07 \dagger	33.43	33.95	<u>15.74</u>	19.37	<u>21.09</u>	1.72	24.72
XLSR+MoE [40]	-	-	0.74	2.96	2.54	-	-	-	-	-	-	-	-	-
XLSR+R+STCA+LMDC [41]	-	-	0.09	0.78	1.87	-	-	-	-	-	-	-	-	-
XLSR+Mamba [42]	319	6.70	0.421	0.93 \dagger	1.88 \dagger	14.40 \dagger	6.71	35.26 \dagger	34.22	19.36	21.84	20.15	2.15 \dagger	24.26
XLSR+BiCrossMamba [43]	318.21	7.94	0.71	3.83	2.35	<u>13.67</u>	6.85	37.70	30.44	18.69	29.44	29.93	<u>2.12</u>	27.36
Wave2Vec2+AASIST(Baseline)	317.84	7.58	0.26	2.48	4.08	13.38	4.24	40.22	33.79	16.14	25.55	22.21	6.96	32.02
HyperPotter	317.87	5.72 <u>11.86</u>	0.23 <u>10.03</u>	3.94 <u>11.46</u>	1.78 <u>12.30</u>	16.04 <u>12.66</u>	3.89 <u>0.35</u>	34.47 <u>5.75</u>	32.34 \dagger <u>11.45</u>	11.31 <u>14.83</u>	21.49 <u>14.06</u>	21.84 \dagger <u>10.37</u>	2.55 <u>14.41</u>	27.71 <u>14.31</u>

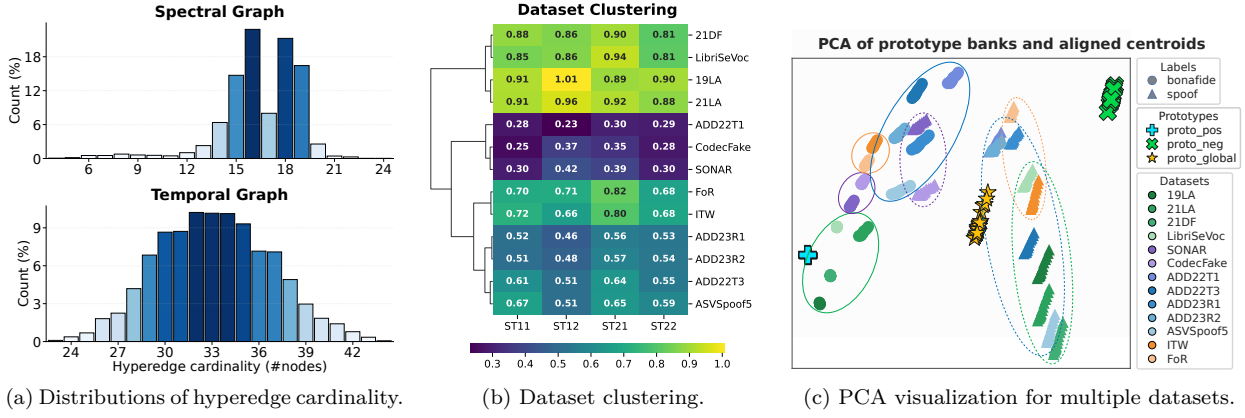


Figure 3: Visualizations demonstrating the effectiveness of HOI modeling and its capability to describe synthetic artifacts.

Slot Alignment enables every centroid to contribute to the corresponding prototype slots in a direct and precise manner. First, centroids from all batches are flattened into a sequence $\mathcal{C} = \{\mathbf{c}_m\}_{m=1}^M$, where $M = B \cdot K$. To align the flattened centroids with the prototypes, we compute assignment weights as $a_{mk} = \text{softmax}(\cos(\mathbf{c}_m^{(g)} \cdot \mathbf{p}_k^{(g)}))$. Based on these assignments, the k -th batch-level global centroid is constructed as:

$$\tilde{\mathbf{c}}_k^{(g)} = \frac{\sum_{m=1}^M a_{mk} \mathbf{c}_m}{\sum_{m=1}^M a_{mk}}$$

The resulting slotted centroids are then fused with the average centroids $\hat{\mathbf{c}}_k^{(g)}$ (as defined in equation 4): $\tilde{\mathbf{c}}_k^{(g)} = (\hat{\mathbf{c}}_k^{(g)} + \hat{\mathbf{c}}_k^{(g)})/2$ to improve robustness.

EMA-based Update Mechanism. To maintain cross-batch stability, the class-conditional prototypes are updated via an EMA: $\hat{\mathbf{P}}^{(+)} = \mu \tilde{\mathbf{C}}^{(+)} + (1 - \mu) \mathbf{P}^{(+)}$, where μ denotes the momentum coefficient. The final global prototypes are computed as: $\hat{\mathbf{P}}^{(g)} = \mu(\gamma \tilde{\mathbf{C}}^{(g)} + (1 - \gamma) \mathbf{N}) + (1 - \mu) \mathbf{P}^{(g)}$. Here, $\mathbf{N} = 0.5(\hat{\mathbf{P}}^{(+)} + \hat{\mathbf{P}}^{(-)})$ represents a class-unbiased neural prototype. This formulation effectively fuses local structural cues with unbiased long-term anchors.

6 Experiments

In this section, we evaluate the generalization performance of the HyperPotter framework across multiple datasets and demonstrate that HOIs are effectively captured and leveraged to describe synthetic artifacts across diverse scenarios.

6.1 Experimental Setup

Datasets and Evaluation Metrics. All models are trained only on the ASVspoof2019 LA training set. Following the evaluation protocol of the Speech DF Arena [7], we evaluate model performance on 13 test sets. These datasets are categorized by language, source dataset, codec, and spoofing method, with detailed descriptions provided in Appendix C. We report Equal Error Rate (EER) and F1 score as evaluation metrics.

Implementation Details. Wav2Vec2-AASIST is used as the backbone, with its graph builder and readout mechanism preserved. Guided by prototype banks, two HAGNN layers are applied to spectral and temporal graphs, respectively. Similar to the HS-GALs in AASIST, we implement four heterogeneous HAGNN layers to model spectral-temporal heterogeneous graphs.

A warm-start mechanism is employed during training to control prototype learning and usage. K-Means is used to initialize FCM and is replaced with prototypes at the 5th epoch. At the first training batch, all prototypes are initialized with the mean of centroids ($\hat{\mathbf{c}}_k^{(g)}$ in Eq. 4). Prototypes are updated using the soft alignment before the 20th epoch, and followed by the slot alignment algorithm in later stages. Starting at epoch 5, the similarity gate τ decays linearly from 0.1 to 0. During evaluation, prototypes remain fixed to avoid information pollution. Other implementation settings are provided in Appendix B. The code and pre-trained models are available at <https://anonymous.4open.science/r/HyperPotter-6C052325>.

6.2 Generalization Performance

Comparison with SOTAs. To ensure a fair comparison, we evaluate HyperPotter against current SOTA models with comparable model sizes (approximately 300M-400M parameters). We also retrain the baseline model, Wav2Vec2-AASIST, under the same training settings as HyperPotter to assess the performance gains accurately. The EER and F1-score results are shown in Table 1 and Table 5. HyperPotter achieves the best EER on several challenging datasets, including In-the-Wild (5.72%), ASVspoof2021 DF (1.78%), FoR (3.89%), and ADD2022 Track3 (11.31%). These datasets represent diverse speakers, varied spoofing attacks, and challenging real-world, cross-lingual conditions. On the remaining datasets, HyperPotter also demonstrates competitive performance. With only 0.03M additional parameters, HyperPotter outperforms the baseline on most datasets. Moderate performance degradation is observed on the 2021LA and ASVspoof5 datasets, where speech samples are heavily affected by diverse codec-based compression and transmission processes. We hypothesize that such distortions act as “masks” that obscure high-order interdependences across the temporal and spectral domains. To enhance HyperPotter under severe channel interference, we explore different codec augmentation strategies, with results shown in Table 7.

Overall, these results suggest that while severe channel interference can mask high-order relational structures, HyperPotter excels in scenarios where speech signals maintain structural integrity—even amidst the complexity of diverse spoofing algorithms and multiple speakers. This distinctive specialization positions HyperPotter as a critical “specialist” in modern anti-spoofing ecosystems. Such a role aligns well with the ongoing shift in practical ADD systems toward ensemble or Multi-Expert (MoE) frameworks for diverse deployment conditions.

6.3 Representation Capability for High-order Relations

Distribution of Hyperedge Cardinality. The cardinality is defined as the number of nodes connected by a hyperedge. To provide evidence for the presence of HOIs, we analyze the distribution of hyperedge cardinalities, followed by a hyperedge pruning with effective membership values larger than $1/\mathcal{D}$ to ensure a clear and meaningful observation. Figure 3a illustrates the results for the spectral and temporal HAGNN blocks, which consist of 42 and 66 total nodes, respectively. We observe that most cardinalities are concentrated around the median node count, indicating HyperPotter tends to capture high-order connections involving multiple nodes selectively rather than relying solely on pairwise interactions (e.g., cardinality of 2).

Data Clustering based on Relational Connections. To evaluate the synthetic discriminability of HOIs, we investigate relational similarity patterns based on hyperedges at both dataset and sample levels. We extract HAGNN centroids from test samples and compute cosine similarities to positive and negative prototypes of bona-fide and spoof classes, from which sample–prototype distribution gaps are derived for each evaluation dataset. Inter-dataset relational similarities are visualized using a clustermap (Figure 3b),

Table 2: Ablation study on HyperPotter sub-modules and alignment algorithms, reported as EERs (%).

	ITW	21LA	21DF	ASV5	FoR
HyperPotter	5.72	3.94	1.78	16.04	3.89
w/o Amplification Module	6.9 \uparrow	3.50 \downarrow	1.88 \uparrow	14.46 \downarrow	6.45 \uparrow
w/o Prototype Banks	6.49 \uparrow	2.80 \downarrow	1.88 \uparrow	15.42 \downarrow	4.59 \uparrow
w/o Both Alignment Algs	5.95 \uparrow	3.83 \downarrow	2.25 \uparrow	19.07 \uparrow	4.46 \uparrow
w/o Soft Alignment Alg	7.45 \uparrow	3.25 \downarrow	2.05 \uparrow	19.42 \uparrow	4.02 \uparrow
w/o Slot Alignment Alg	6.18 \uparrow	3.24 \downarrow	2.07 \uparrow	19.90 \uparrow	4.02 \uparrow

where hierarchical clustering across four HAGNN layers groups datasets with similar patterns closer together. The resulting clustering structure is consistent with our analysis of dataset generation mechanisms in Table 4. At the embedding level, we visualize the prototype banks and slot-aligned centroids using PCA (Figure 3c), where datasets are categorized by data source: traditional deepfake data (green), neural codec data (purple), complex and unspecified data (blue), and online data (orange). Solid and dashed lines denote bona-fide and spoof data, respectively. We observe that bona-fide centroids from similar sources exhibit close distribution, while spoofing centroids from different data types are generally clustered in a compact region (with the exception of codec data[†]). This suggests that high-order relational modeling effectively captures shared spoofing characteristics across diverse datasets. More details about our metric and sample-level analyses are provided in the Appendix F.

6.4 Ablation Studies

Influence of HyperPotter Sub-modules. We conduct an ablation study on the sub-modules of HyperPotter and alignment algorithms, as shown in Table 2. Performance degradation is observed when key components are removed, especially under real-world conditions (ITW and FoR) and diverse spoofing attacks (21DF), demonstrating the importance of these modules in effective HOI modeling. The convergence behavior of different models are shown in Figure 6. Although the inclusion of HAGNN blocks slows down convergence, introducing prototype banks alleviates this issue and improves training efficiency.

Table 3: Comparison of different hyperedge counts (K) and degrees (\mathcal{D}), evaluated using EER (%). N denotes the number of nodes in the input graph.

	ITW	21LA	21DF	ASVspoof5	FoR
HyperPotter	5.72	3.94	1.78	16.04	3.89
$K = 0.25N$	5.88 \uparrow	3.63 \downarrow	1.92 \uparrow	18.23 \uparrow	4.06 \uparrow
$K = 0.50N$	6.39 \uparrow	2.87 \downarrow	1.76 \downarrow	19.00 \uparrow	4.77 \uparrow
$K = 0.75N$	6.09 \uparrow	3.37 \downarrow	1.76 \downarrow	19.22 \uparrow	4.86 \uparrow
$\mathcal{D} = 0.25N$	4.97 \downarrow	3.44 \downarrow	1.60 \downarrow	18.89 \uparrow	5.61 \uparrow
$\mathcal{D} = 0.50N$	5.97 \uparrow	2.71 \downarrow	2.04 \uparrow	17.74 \uparrow	3.93 \uparrow
$\mathcal{D} = 0.75N$	6.02 \uparrow	2.44 \downarrow	1.96 \uparrow	16.91 \uparrow	3.75 \downarrow
$\mathcal{D} = 2$	6.95 \uparrow	3.79 \downarrow	2.20 \uparrow	20.04 \uparrow	5.21 \uparrow

Influence of Hyperedge Counts and Degrees. The number and degree of hyperedges, corresponding to the FCM cluster count and membership degree, directly determine the hypergraph structure. The results are reported in Table 3, indicating that HyperPotter adopts hyperedge counts of 25% N –50% N with degree-free settings as a reasonable trade-off. Smaller \mathcal{D} imposes overly strict constraints on HOIs, delivering superior results under advantageous conditions, while $\mathcal{D} = 2$ reduces the hypergraph to a pairwise graph and leads to performance degradation. These results underscore the necessity of HOIs, especially in enhancing ADD performance under complex scenarios characterized by diverse spoofing algorithms and multiple speakers.

[†]The role of neural codec methods is not clearly defined, as it may be viewed either as augmentation methods in ASVspoof5 or as spoofing mechanisms in CodecFake.

7 Conclusion

This paper investigates audio deepfake detection from a high-order interaction perspective and demonstrates that discriminative synthetic artifacts are dominated by synergistic dependencies beyond pairwise correlations. Using O-information, we provide evidence for the importance of high-order synergy in capturing generalizable deepfake cues. To model such effects, we propose HyperPotter, a prototype-oriented hypergraph framework that explicitly represents multi-way relations and amplifies informative synergistic artifacts. Extensive experiments on 13 datasets show that HyperPotter consistently improves cross-scenario generalization, achieving an average relative gain of 15.32%.

References

- [1] Kun Wang, Meng Chen, Li Lu, Jingwen Feng, Qianniu Chen, Zhongjie Ba, Kui Ren, and Chun Chen. From one stolen utterance: Assessing the risks of voice cloning in the aigc era. In *2025 IEEE Symposium on Security and Privacy (SP)*, pages 4663–4681, 2025.
- [2] Siwei Lyu. Deepfakes leveled up in 2025: Here’s what’s coming next. <https://theconversation.com/deepfakes-leveled-up-in-2025-heres-whats-coming-next-271391>, December 2025. [Online; accessed 2026-01-18].
- [3] Melissa Brown. Football and media personality eddie mcguire used in deepfake financial advertisement. <https://www.abc.net.au/news/2025-03-31/vic-eddie-mcguire-deepfake-video-financial-scam/105115764>, March 2025. [Online; accessed 2026-01-18].
- [4] NPR. Impostor ai impersonates rubio, contacts foreign officials. <https://www.npr.org/2025/07/09/nx-s1-5462195/impostor-ai-impersonate-rubio-foreign-officials>, July 2025. [Online; accessed 2026-01-18].
- [5] Hemlata Tak, Jose Patino, Massimiliano Todisco, Andreas Nautsch, Nicholas Evans, and Anthony Larcher. End-to-end anti-spoofing with rawnet2. In *ICASSP 2021 - 2021 IEEE International Conference on Acoustics, Speech and Signal Processing (ICASSP)*, pages 6369–6373, 2021.
- [6] J. W. Jung, H. S. Heo, H. Tak, H. J. Shim, J Son Chung, B. J. Lee, H. J. Yu, and N. Evans. Aasist: Audio anti-spoofing using integrated spectro-temporal graph attention networks. In *arXiv e-prints*, 2021.
- [7] Sandipana Dowerah, Atharva Kulkarni, Ajinkya Kulkarni, Hoan My Tran, Joonas Kalda, Artem Fedorchenko, Benoit Fauve, Damien Lalive, Tanel Alumäe, and Matthew Magimai Doss. Speech df arena: A leaderboard for speech deepfake detection models. *arXiv preprint arXiv:2509.02859*, 2025.
- [8] Federico Battiston, Enrico Amico, Alain Barrat, Ginestra Bianconi, Guilherme Ferraz de Arruda, Benedetta Franceschiello, Iacopo Iacopini, Sonia Kéfi, Vito Latora, Yamir Moreno, et al. The physics of higher-order interactions in complex systems. *Nature physics*, 17(10):1093–1098, 2021.
- [9] Fernando Rosas, Pedro AM Mediano, Michael Gastpar, and Henrik J Jensen. Quantifying high-order interdependencies via multivariate extensions of the mutual information. *arXiv preprint arXiv:1902.11239*, 2019.
- [10] Tanvina B Patel and Hemant A Patil. Combining evidences from mel cepstral, cochlear filter cepstral and instantaneous frequency features for detection of natural vs. spoofed speech. In *Sixteenth annual conference of the international speech communication association*, 2015.
- [11] Steven Davis and Paul Mermelstein. Comparison of parametric representations for monosyllabic word recognition in continuously spoken sentences. *IEEE transactions on acoustics, speech, and signal processing*, 28(4):357–366, 1980.
- [12] Massimiliano Todisco, Héctor Delgado, and Nicholas Evans. Constant q cepstral coefficients: A spoofing countermeasure for automatic speaker verification. *Computer Speech & Language*, 45:516–535, 2017.

- [13] Hemlata Tak, Jee-weon Jung, Jose Patino, Madhu Kamble, Massimiliano Todisco, and Nicholas Evans. End-to-end spectro-temporal graph attention networks for speaker verification anti-spoofing and speech deepfake detection. *arXiv preprint arXiv:2107.12710*, 2021.
- [14] Xin Wang and Junichi Yamagishi. Investigating self-supervised front ends for speech spoofing countermeasures. *arXiv preprint arXiv:2111.07725*, 2021.
- [15] Hemlata Tak, Massimiliano Todisco, Xin Wang, Jee-weon Jung, Junichi Yamagishi, and Nicholas Evans. Automatic speaker verification spoofing and deepfake detection using wav2vec 2.0 and data augmentation. *arXiv preprint arXiv:2202.12233*, 2022.
- [16] Eros Rosello, Alejandro Gómez Alanís, Angel M Gomez, Antonio M Peinado, N Harte, J Carson-Berndsen, and G Jones. A conformer-based classifier for variable-length utterance processing in anti-spoofing. In *Interspeech*, volume 2023, pages 5281–5285, 2023.
- [17] Mu-Rong Yang and Xin-Jian Xu. Recent advances in hypergraph neural networks: M.-r. yang, x.-j. xu. *Journal of the Operations Research Society of China*, pages 1–37, 2025.
- [18] Yingqi Zhao, Haiwei Zhang, Qijie Bai, Changli Nie, and Xiaojie Yuan. Dhmae: A disentangled hypergraph masked autoencoder for group recommendation. In *Proceedings of the 47th International ACM SIGIR Conference on Research and Development in Information Retrieval*, pages 914–923, 2024.
- [19] Hongjie Chen, Ryan A Rossi, Sungchul Kim, Kanak Mahadik, and Hoda Eldardiry. Probabilistic hypergraph recurrent neural networks for time-series forecasting. In *Proceedings of the 31st ACM SIGKDD Conference on Knowledge Discovery and Data Mining V. 1*, pages 82–93, 2025.
- [20] Sirui Huang, Hanqian Li, Yanggan Gu, Xuming Hu, Qing Li, and Guandong Xu. Hyperg: Hypergraph-enhanced llms for structured knowledge. In *Proceedings of the 48th International ACM SIGIR Conference on Research and Development in Information Retrieval*, pages 1218–1228, 2025.
- [21] Yan Han, Peihao Wang, Souvik Kundu, Ying Ding, and Zhangyang Wang. Vision hgnn: An image is more than a graph of nodes. In *Proceedings of the IEEE/CVF International Conference on Computer Vision*, pages 19878–19888, 2023.
- [22] Caoshuo Li, Tanzhe Li, Xiaobin Hu, Donghao Luo, and Taisong Jin. Dvhggnn: Multi-scale dilated vision hgnn for efficient vision recognition. In *Proceedings of the Computer Vision and Pattern Recognition Conference*, pages 20158–20168, 2025.
- [23] Joshua Fixelle. Hypergraph vision transformers: Images are more than nodes, more than edges. In *Proceedings of the Computer Vision and Pattern Recognition Conference*, pages 9751–9761, 2025.
- [24] Shubhr Singh, Emmanouil Benetos, Huy Phan, and Dan Stowell. Lhggn: Local-higher order graph neural networks for audio classification and tagging. In *ICASSP 2025-2025 IEEE International Conference on Acoustics, Speech and Signal Processing (ICASSP)*, pages 1–5. IEEE, 2025.
- [25] Korawat Tanwisuth, Xinjie Fan, Huangjie Zheng, Shujian Zhang, Hao Zhang, Bo Chen, and Mingyuan Zhou. A prototype-oriented framework for unsupervised domain adaptation. *Advances in Neural Information Processing Systems*, 34:17194–17208, 2021.
- [26] Yingwei Pan, Ting Yao, Yehao Li, Yu Wang, Chong-Wah Ngo, and Tao Mei. Transferrable prototypical networks for unsupervised domain adaptation. In *Proceedings of the IEEE/CVF conference on computer vision and pattern recognition*, pages 2239–2247, 2019.
- [27] Wei Luo, Yunkang Cao, Haiming Yao, Xiaotian Zhang, Jianan Lou, Yuqi Cheng, Weiming Shen, and Wenyong Yu. Exploring intrinsic normal prototypes within a single image for universal anomaly detection. In *Proceedings of the Computer Vision and Pattern Recognition Conference*, pages 9974–9983, 2025.
- [28] Jiahe Tian, Cai Yu, Xi Wang, Peng Chen, Zihao Xiao, Jizhong Han, and Yesheng Chai. Dynamic mixed-prototype model for incremental deepfake detection. In *Proceedings of the 32nd ACM International Conference on Multimedia*, pages 8129–8138, 2024.

[29] Youngsik Eom, Yeonghyeon Lee, Ji Sub Um, and Hoirin Kim. Anti-spoofing using transfer learning with variational information bottleneck. *arXiv preprint arXiv:2204.01387*, 2022.

[30] Federico Battiston, Giulia Cencetti, Iacopo Iacopini, Vito Latora, Maxime Lucas, Alice Patania, Jean-Gabriel Young, and Giovanni Petri. Networks beyond pairwise interactions: Structure and dynamics. *Physics reports*, 874:1–92, 2020.

[31] Devanshu Arya, Deepak K Gupta, Stevan Rudinac, and Marcel Worring. Hypersage: Generalizing inductive representation learning on hypergraphs. *arXiv preprint arXiv:2010.04558*, 2020.

[32] Alessia Antelmi, Gennaro Cordasco, Mirko Polato, Vittorio Scarano, Carmine Spagnuolo, and Dingqi Yang. A survey on hypergraph representation learning. *ACM Computing Surveys*, 56(1):1–38, 2023.

[33] Zhangjie Fu, Fengxiao Huang, Kui Ren, Jian Weng, and Cong Wang. Privacy-preserving smart semantic search based on conceptual graphs over encrypted outsourced data. *IEEE Transactions on Information Forensics and Security*, 12(8):1874–1884, 2017.

[34] Zuheng Kang, Yayun He, Botao Zhao, Xiaoyang Qu, Junqing Peng, Jing Xiao, and Jianzong Wang. Retrieval-augmented audio deepfake detection. In *Proceedings of the 2024 International Conference on Multimedia Retrieval*, pages 376–384, 2024.

[35] Wei Ju, Zhengyang Mao, Siyu Yi, Yifang Qin, Yiyang Gu, Zhiping Xiao, Yifan Wang, Xiao Luo, and Ming Zhang. Hypergraph-enhanced dual semi-supervised graph classification. *arXiv preprint arXiv:2405.04773*, 2024.

[36] Duc-Tuan Truong, Ruijie Tao, Tuan Nguyen, Hieu-Thi Luong, Kong Aik Lee, and Eng Siong Chng. Temporal-channel modeling in multi-head self-attention for synthetic speech detection. In *Proc. Interspeech 2024*, pages 537–541, 2024.

[37] Yuxiang Zhang, Jingze Lu, Zengqiang Shang, Wenchao Wang, and Pengyuan Zhang. Improving short utterance anti-spoofing with aasist2. In *ICASSP 2024-2024 IEEE International Conference on Acoustics, Speech and Signal Processing (ICASSP)*, pages 11636–11640. IEEE, 2024.

[38] Yinlin Guo, Haofan Huang, Xi Chen, He Zhao, and Yuehai Wang. Audio deepfake detection with self-supervised wavlm and multi-fusion attentive classifier. In *ICASSP 2024-2024 IEEE International Conference on Acoustics, Speech and Signal Processing (ICASSP)*, pages 12702–12706. IEEE, 2024.

[39] Qishan Zhang, Shuangbing Wen, and Tao Hu. Audio deepfake detection with self-supervised xls-r and sls classifier. In *Proceedings of the 32nd ACM International Conference on Multimedia*, pages 6765–6773, 2024.

[40] Zhiyong Wang, Ruibo Fu, Zhengqi Wen, Jianhua Tao, Xiaopeng Wang, Yuankun Xie, Xin Qi, Shuchen Shi, Yi Lu, Yukun Liu, et al. Mixture of experts fusion for fake audio detection using frozen wav2vec 2.0. In *ICASSP 2025-2025 IEEE International Conference on Acoustics, Speech and Signal Processing (ICASSP)*, pages 1–5. IEEE, 2025.

[41] Yunqi Hao, Minqiang Xu, Yihao Chen, Yanyan Liu, Liang He, Lei Fang, and Lin Liu. Integrating spectro-temporal cross aggregation and multi-scale dynamic learning for audio deepfake detection. In *ICASSP 2025 - 2025 IEEE International Conference on Acoustics, Speech and Signal Processing (ICASSP)*, pages 1–5, 2025.

[42] Yang Xiao and Rohan Kumar Das. Xlsr-mamba: A dual-column bidirectional state space model for spoofing attack detection. *IEEE Signal Processing Letters*, 2025.

[43] Yassine El Kheir, Tim Polzehl, and Sebastian Möller. BiCrossMamba-ST: Speech Deepfake Detection with Bidirectional Mamba Spectro-Temporal Cross-Attention. In *Interspeech 2025*, pages 2235–2239, 2025.

[44] Arun Babu, Changhan Wang, Andros Tjandra, Kushal Lakhotia, Qiantong Xu, Naman Goyal, Kritika Singh, Patrick von Platen, Yatharth Saraf, Juan Pino, et al. Xls-r: Self-supervised cross-lingual speech representation learning at scale. *arXiv preprint arXiv:2111.09296*, 2021.

[45] Hemlata Tak, Madhu Kamble, Jose Patino, Massimiliano Todisco, and Nicholas Evans. Rawboost: A raw data boosting and augmentation method applied to automatic speaker verification anti-spoofing. In *ICASSP 2022-2022 IEEE International Conference on Acoustics, Speech and Signal Processing (ICASSP)*, pages 6382–6386. IEEE, 2022.

[46] Daniel S Park, William Chan, Yu Zhang, Chung-Cheng Chiu, Barret Zoph, Ekin D Cubuk, and Quoc V Le. Specaugment: A simple data augmentation method for automatic speech recognition. *arXiv preprint arXiv:1904.08779*, 2019.

[47] David Snyder, Guoguo Chen, and Daniel Povey. Musan: A music, speech, and noise corpus. *arXiv preprint arXiv:1510.08484*, 2015.

[48] Massimiliano Todisco, Xin Wang, Ville Vestman, Md Sahidullah, Hector Delgado, Andreas Nautsch, Junichi Yamagishi, Nicholas Evans, Tomi Kinnunen, and Kong Aik Lee. ASVspoof 2019: Future horizons in spoofed and fake audio detection. *arXiv preprint arXiv:1904.05441*, 2019.

[49] Nicolas M Müller, Pavel Czempin, Franziska Dieckmann, Adam Froghyar, and Konstantin Böttinger. Does audio deepfake detection generalize? *Interspeech*, 2022.

[50] Junichi Yamagishi, Xin Wang, Massimiliano Todisco, Md Sahidullah, Jose Patino, Andreas Nautsch, Xuechen Liu, Kong Aik Lee, Tomi Kinnunen, Nicholas Evans, et al. Asvspoof 2021: accelerating progress in spoofed and deepfake speech detection. *arXiv preprint arXiv:2109.00537*, 2021.

[51] Xin Wang, Héctor Delgado, Hemlata Tak, Jee-weon Jung, Hye-jin Shim, Massimiliano Todisco, Ivan Kukanov, Xuechen Liu, Md Sahidullah, Tomi Kinnunen, et al. Asvspoof 5: Crowdsourced speech data, deepfakes, and adversarial attacks at scale. *arXiv preprint arXiv:2408.08739*, 2024.

[52] Ricardo Reimao and Vassilios Tzerpos. For: A dataset for synthetic speech detection. In *2019 International Conference on Speech Technology and Human-Computer Dialogue (SpeD)*, pages 1–10. IEEE, 2019.

[53] Yuankun Xie, Yi Lu, Ruibo Fu, Zhengqi Wen, Zhiyong Wang, Jianhua Tao, Xin Qi, Xiaopeng Wang, Yukun Liu, Haonan Cheng, et al. The codecfake dataset and countermeasures for the universally detection of deepfake audio. *IEEE Transactions on Audio, Speech and Language Processing*, 2025.

[54] Jiangyan Yi, Ruibo Fu, Jianhua Tao, Shuai Nie, Haoxin Ma, Chenglong Wang, Tao Wang, Zhengkun Tian, Ye Bai, Cunhang Fan, et al. Add 2022: the first audio deep synthesis detection challenge. In *ICASSP 2022-2022 IEEE International Conference on Acoustics, Speech and Signal Processing (ICASSP)*, pages 9216–9220. IEEE, 2022.

[55] Jiangyan Yi, Jianhua Tao, Ruibo Fu, Xinrui Yan, Chenglong Wang, Tao Wang, Chu Yuan Zhang, Xiaohui Zhang, Yan Zhao, Yong Ren, et al. Add 2023: the second audio deepfake detection challenge. *arXiv preprint arXiv:2305.13774*, 2023.

[56] Chengzhe Sun, Shan Jia, Shuwei Hou, and Siwei Lyu. Ai-synthesized voice detection using neural vocoder artifacts. In *Proceedings of the IEEE/CVF Conference on Computer Vision and Pattern Recognition*, pages 904–912, 2023.

[57] Xiang Li, Pin-Yu Chen, and Wenqi Wei. Where are we in audio deepfake detection? a systematic analysis over generative and detection models, 2025.

[58] Lin Zhang, Xin Wang, Erica Cooper, Nicholas Evans, and Junichi Yamagishi. The partialspoof database and countermeasures for the detection of short fake speech segments embedded in an utterance. *IEEE/ACM Transactions on Audio, Speech, and Language Processing*, 31:813–825, 2022.

A Baselines: AASIST-related Networks

AASIST [6] is a spectral-temporal graph neural network, one of the most competitive models without using SSL front-ends. The raw waveform is fed into convolution filters in the SincNet layer first. Then the following RawNet2-based residual encoder produces a high-level representation. A max-pooling operation is applied to extract both temporal and spectral representations. The representations are fed into graph attention and graph pooling layers and merged into a heterogeneous spectral-temporal graph. The heterogeneous information is integrated into stack nodes in the heterogeneous stacking graph attention layers (HS-GALs). A max graph operation is applied to the outputs of HS-GAL to produce an advanced heterogeneous graph. Derived through the node-wise maximum and average operations over the graph, nodes are concatenated and fed into an FC layer to produce outputs.

Wav2Vec2-AASIST [15] combines an informative SSL front-end and an AASIST classifier, achieving the SOTA performance. The front-end is a pre-trained wav2vec2 model XLS-R (0.3B) [44]. The XLS-R model includes a convolutional encoder and a BERT-structured transformer. During pre-training, the discretized CNN encoder output is masked and fed into the transformer to generate the context output. A contrastive task for context output is conducted to distinguish the true discretized latent from distractors sampled from other time steps. The XLS-R model is pre-trained on 436K hours of bona-fide speech data in 128 languages. The back-end of Wav2Vec2-AASIST follows AASIST and consists of a RawNet2 encoder and graph-based modules.

B More Implementation details.

For FCM, the fuzzifier m and the maximum iteration number are set to 2 and 5, respectively. The fusion balancing factors β_1, β_2 are set as 0.9 and 0.6. We set the batch size to 96. The model is trained for 100 epochs, and the checkpoint achieving the best performance on the In-The-Wild (ITW) test set is selected. This is because ITW is a more balanced and representative benchmark that better reflects the real generalization capability of the checkpoints, whereas the ASVspoof 2019 LA development set consistently yields a 0% EER. Three data augmentation methods are applied: Rawboost (option 5: linear and non-linear convulsive noise and impulsive signal-dependent additive noise in series) [45], SpecAugment [46], and MUSAN [47]. All experiments are conducted on two NVIDIA H800 GPUs.

Other experimental settings follow the released Wav2Vec2-AASIST codebase. We use the pretrained XLS-R 300M as our front-end. All audio samples are either padded or truncated to 4 seconds (64,000 samples). We adopt the AdamW optimizer with a learning rate of 1e-6 and a weight decay of 1e-4. The random seed is fixed to 1234. We employ a weighted cross-entropy loss to address the class imbalance in the ASVspoof 2019 LA training set, assigning a weight of 0.9 to the bona-fide class and 0.1 to the spoof class.

C Datasets

Following a similar evaluation protocol to the Speech DF Arena leaderboard [7], we conduct experiments on 13 test sets, including ASVspoof 2019 LA [48], In-the-Wild [49], ASVspoof 2021 LA, ASVspoof 2021 DF [50], ASVspoof2024 [51], For [52], Codecfake [53], ADD2022 Track 1 and Track 3 [54], ADD2023 Track1.2 Round 1 and Round 2 [55], LibriVoc [56], and SONAR [57]. The DFADD dataset is excluded due to a mismatch between its data format and our detection model.

Table 4: Summary of speech spoofing datasets used in this work.

Dataset	Language	Source Dataset	Codec	Spoofing Methods
19LA	English	VCTK	no	Traditional TTS/VC
21LA	English	VCTK	Telephony/VoIP codecs	Traditional TTS/VC
21DF	English	VCTK	Compressed audio	Diverse TTS/VC
LibriVoc	English	LibriTTS	no	Neural vocoders
ADD2022T1	Chinese	AISHELL	no	Unspecified and complex
ADD2022T3	Chinese	AISHELL	no	Unspecified and complex

Dataset	Language	Source Dataset	Codec	Spoofing Methods
ADD2023T1.2R1	Chinese	AISHELL, THCHS-30	no	Unspecified and complex
ADD2023T1.2R2	Chinese	AISHELL, THCHS-30	no	Unspecified and complex
ASVSpoof5	English	MLS-English	Multiple codecs	complex TTS/VC
In-The-Wild	English	Public figures (online)	no	Online video segmentation
For SONAR	English	online resource	no	Commercial/public TTS
CodecFake	Mixed	online resource	no	TTS incl. codec-based
		LibriTTS, VCTK, AISHELL	no	Neural codec models

D F1 score Comparison of Different Models

Baseline models for which F1-scores are not reported in the original papers are excluded from the table.

Table 5: F1-score (%) comparison on multiple evaluation sets. Higher is better. **Bold**, underline, and \dagger indicate the best, second-best, and third-best results, respectively.

Model	Params (M)	In-the-Wild	ASV20 19LA	ASV20 21LA	ASV20 21DF	ASV20 24	FoR	Codecfake	ADD22 Track1	ADD22 Track3	ADD23 R1	ADD23 R2	Libri Voc	SONAR
Wav2Vec2+AASIST [15]	317.84	90.9	<u>98.9</u>	96.0	44.0	67.7	92.6	44.3	<u>56.0</u>	62.3	78.8	84.0	69.3	57.4
XLSR+Conformer+TCM [36]	319	93.7	99.1	86.6	71.8	63.7	89.3	52.0	49.0	<u>55.3</u>	82.4	83.4	92.2	76.1 \dagger
XLSR+BiCrossMamba [43]	318.21	93.6	96.7	83.4	69.9	<u>72.0</u>	93.1	50.1	56.7	58.8	77.4	77.6	<u>92.9</u>	75.3
XLSR+SLS [39]	340	94.0 \dagger	<u>98.9</u>	87.1	74.1 \dagger	63.8	94.9 \dagger	54.8	52.8	<u>63.7</u>	85.6	<u>84.7</u>	93.4	<u>77.8</u>
XLSR+Mamba [42]	319	<u>94.6</u>	98.0	<u>95.5</u>	74.4	70.8 \dagger	93.3	52.8 \dagger	52.4	57.7	83.6 \dagger	85.4	92.6 \dagger	78.2
Wav2Vec2+AASIST (Baseline)	317.84	93.9	98.8 \dagger	88.7 \dagger	56.7	72.5	<u>95.8</u>	47.5	52.9	63.0 \dagger	80.6	83.8	79.3	71.0
HyperPotter	317.87	95.4 \dagger 1.5	<u>98.9</u> \dagger 0.1	83.0 \dagger 5.7	75.4 \dagger 18.7	68.1 \dagger 4.4	96.1 \dagger 0.3	<u>53.7</u> \dagger 6.2	54.6 \dagger \dagger 1.7	72.0 \dagger 9.0	<u>83.9</u> \dagger 3.3	84.1 \dagger \dagger 0.3	91.6 \dagger 1.2 \dagger 3	75.0 \dagger 4.0

E Generalization performance across diverse scenarios

Table 6: Comparison of F1-scores (%) between Pairwise (Baseline) and High-order (HyperPotter) interactions across different scenarios. Each scenario contains multiple datasets, and the performance is reported as the mean F1 score across these datasets.

Scenario	Dataset(s)	Pairwise (Baseline)	HOI (HyperPotter)
Online Data	ITW, FoR, SONAR	86.9	88.8
Various Attacks	ADD22T1, ADD22T3, ADD23R1, ADD23R2, 21DF	67.4	74.0
Cross-Lingual	ADD22T1, ADD22T3, ADD23R1, ADD23R2, CodecFake, SONAR	64.7	70.6
Strong Distortion	21LA, ASV2024	80.1	75.6
Varied Speakers	LibriVoc	79.3	91.6

Table 6 compares the F1-scores of the baseline model (Pairwise) and the proposed HyperPotter (HOI) across different scenarios. HyperPotter consistently outperforms the baseline in most scenarios, particularly in “Various Attacks”, “Cross-Lingual”, and “Varied Speakers”. However, in the “Strong Distortion” scenario, HyperPotter shows a decrease in performance compared to the baseline. These results are visualized in Figure 1, which plots the F1-scores of both models across all scenarios, with the coordinate range set from 50% to 100%, and the visualization is shown on the right side of the figure.

F Visualization for sample-level relations.

To investigate the relational segments at the sample-level, we conduct experiments using the PartialSpoof dataset [58]. Specifically, we filter the dataset for utterances exceeding 5 s in duration that contain both bona-fide and spoofed segments. The audio waveforms are segmented into 0.64 s windows, for each of which a gap score is computed. Specifically, we extract HAGNN centroids from test segments and compute their cosine similarities to positive and negative prototypes for bona-fide and spoof classes. Based on these similarities, we define a distribution gap metric as $gap = (s_{bp} + s_{sn} - s_{bn} - s_{sp})/2$, which measures the relative discrepancy between class prototypes and segment representations. To assess inter-segment similarities, we generate clustermaps (Fig. 4) to illustrate correlations via some representative samples, where deeper yellow intensity denotes higher similarity. The clustermap is accompanied by two color-coded sidebars: the outer bar

represents the ground truth, while the inner bar indicates the predicted gap scores (blue for bona fide, red for spoof). For each utterance, we further apply K-Means clustering to the gap scores of all segments, where $k = 2$. The mean value of gap scores from the two cluster centroids is used as the classification threshold to distinguish bona-fide and spoofed segments. The corresponding classification results for the representative samples are illustrated in Fig. 5.

G Impact of Codec Augmentations.

To enhance HyperPotter under severe channel interference, multiple codec strategies are investigated. The results are reported in Table 7. The conflicting performance trends between ITW and ASVspoof5 indicate codec-based methods improve performance in matched noisy conditions, while potentially interfering with HOI modeling and its generalization.

Table 7: Comparison of HyperPotter augmented with different codec strategies, reported as EERs (%).

	ITW	21LA	ASV5	ADD22T1	Codecfake
HyperPotter	5.72	3.94	16.04	32.34	34.47
+speex	7.77 \uparrow	1.61 \downarrow	10.62 \downarrow	31.94 \downarrow	38.84 \uparrow
+opus	11.63 \uparrow	2.90 \downarrow	10.11 \downarrow	30.29 \downarrow	37.37 \uparrow
+Encodec	9.08 \uparrow	2.19 \downarrow	12.03 \downarrow	31.71 \downarrow	39.42 \uparrow

H Ablation Study for SSL-based front-end.

Table 8: Ablation results of replacing the HtrgGraphAttentionLayer in AASIST with HGNN and HGNN Memory (EER, %)

Model	ITW	19LA	21LA	21DF	ASVsopof5
AASIST	43.01	0.83	11.46	21.07	35.53
AASIST + HGNN	43.52 \uparrow	2.48 \uparrow	8.13 \downarrow	20.01 \downarrow	35.01 \downarrow
AASIST + HGNN Memory	38.65 \downarrow	3.10 \uparrow	10.66 \downarrow	18.64 \downarrow	35.30 \downarrow

Table 8 reports the ablation results obtained by replacing the HtrgGraphAttentionLayer in AASIST with the proposed HAGNN layer. To ensure fair comparison, all ablation experiments strictly follow the same training strategy and hyperparameter settings as used in AASIST, without any task-specific tuning for the newly introduced modules. Despite this, the proposed components consistently improve performance on several challenging benchmarks, including 21LA, 21DF, ASVsopof5, and ITW, demonstrating the effectiveness of hypergraph modeling and the prototype-based memory mechanism. Meanwhile, performance degradation is observed on certain in-domain datasets (e.g., 19LA), suggesting that further optimization of hyperparameters may lead to more consistent gains.

I More Figures and Tables

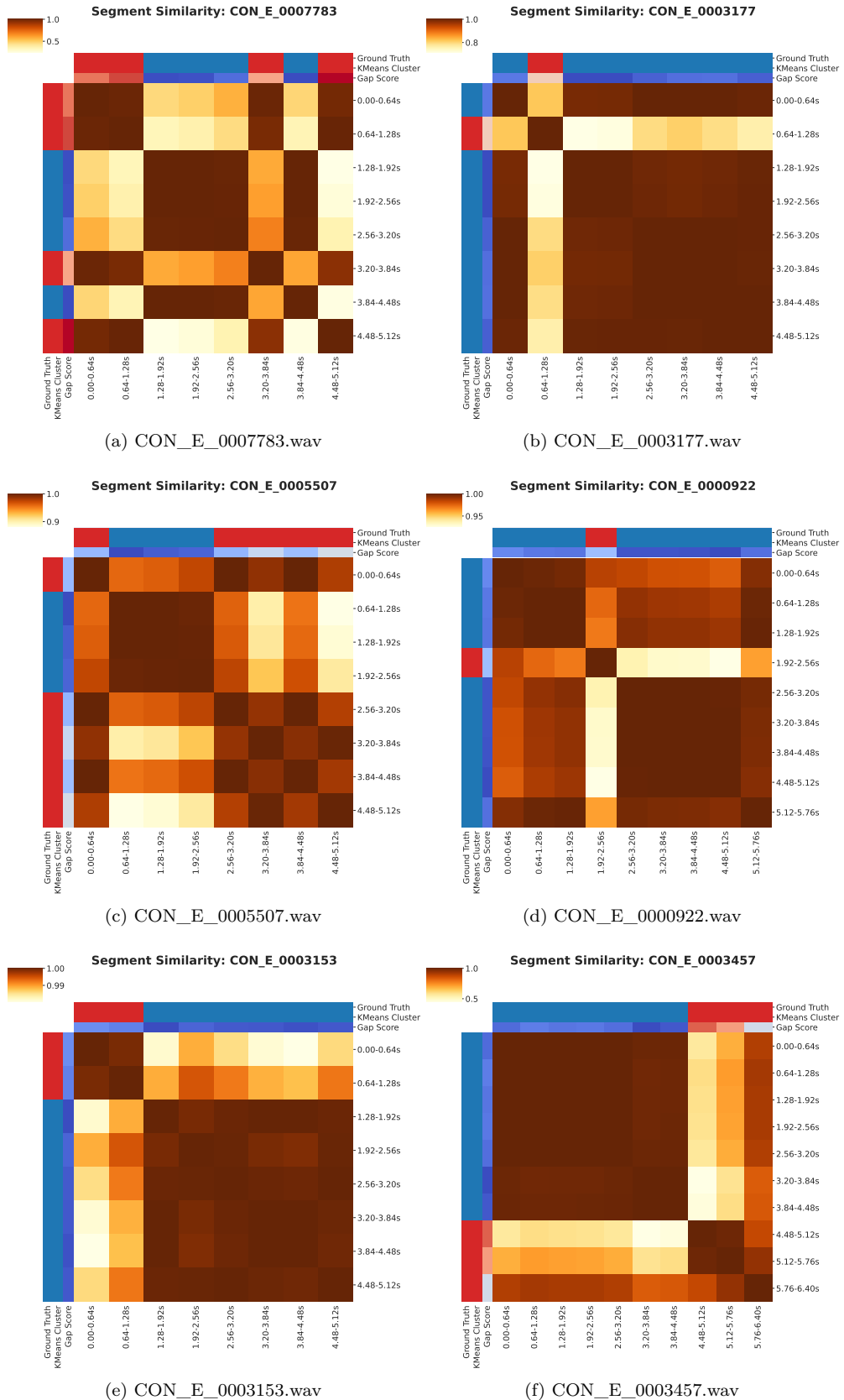


Figure 4: Clustermaps for different samples in PartialSpoof evaluation set

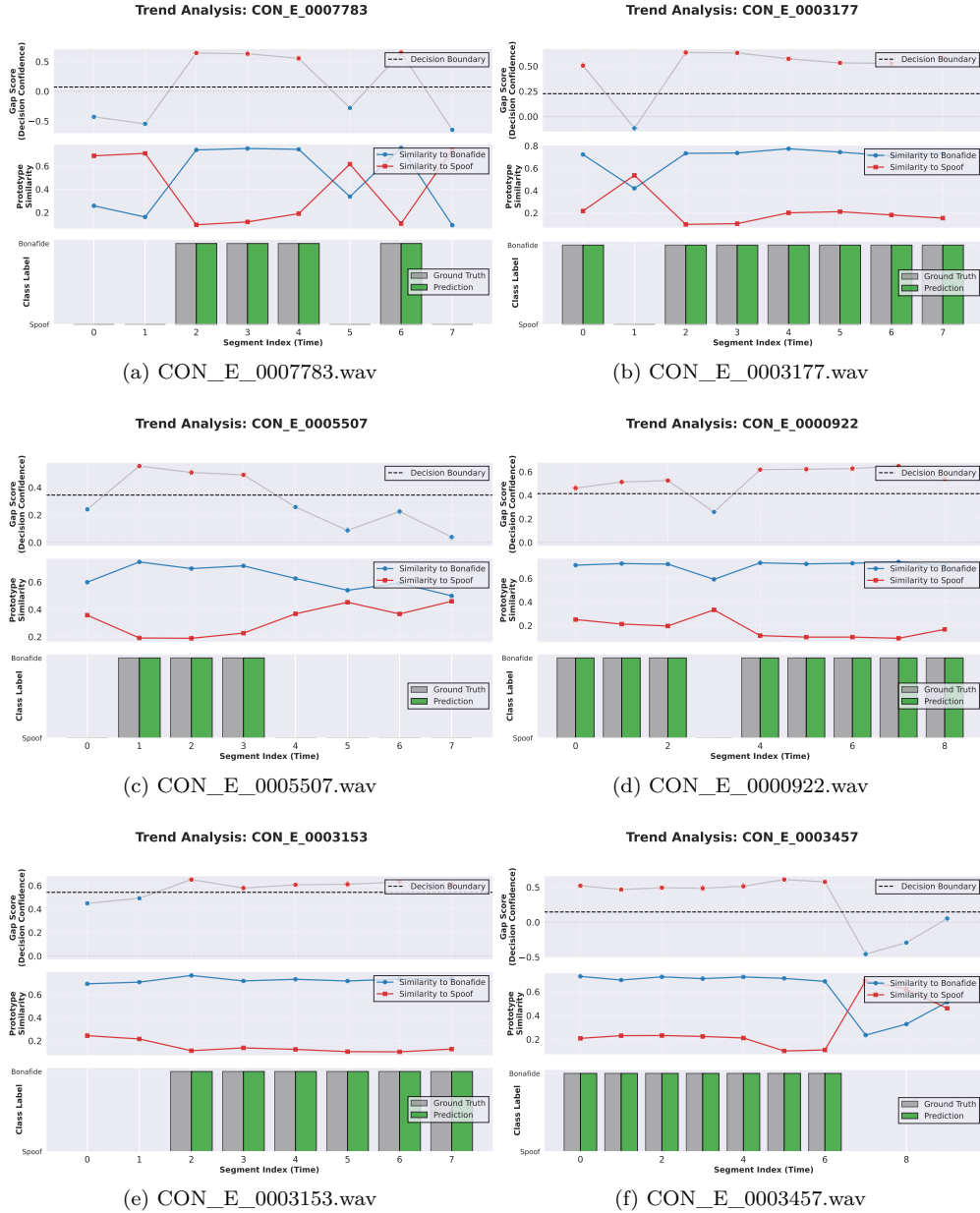


Figure 5: Classification results based on the distribution of centroids for different samples in PartialSpoof evaluation set

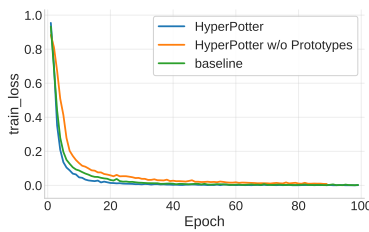


Figure 6: Comparison of convergence speed across different detection models.

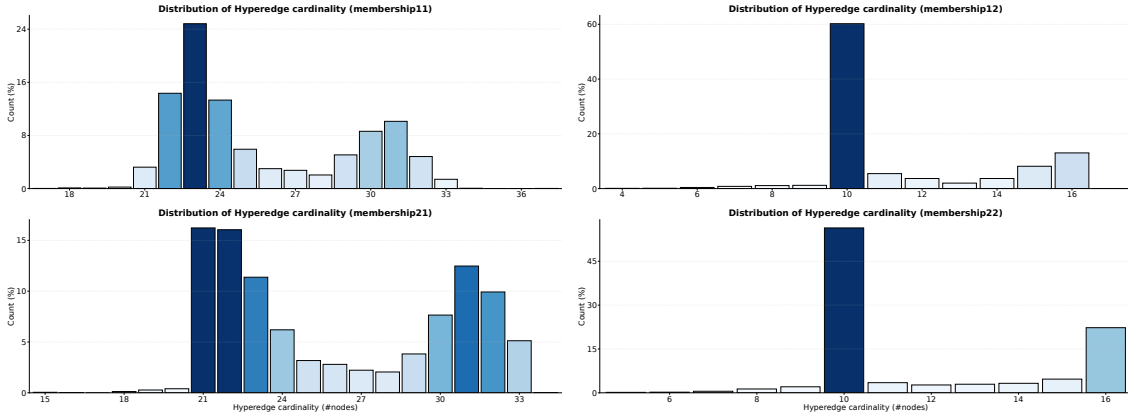


Figure 7: Distributions of hyperedge cardinality for four heterogeneous graph layers.

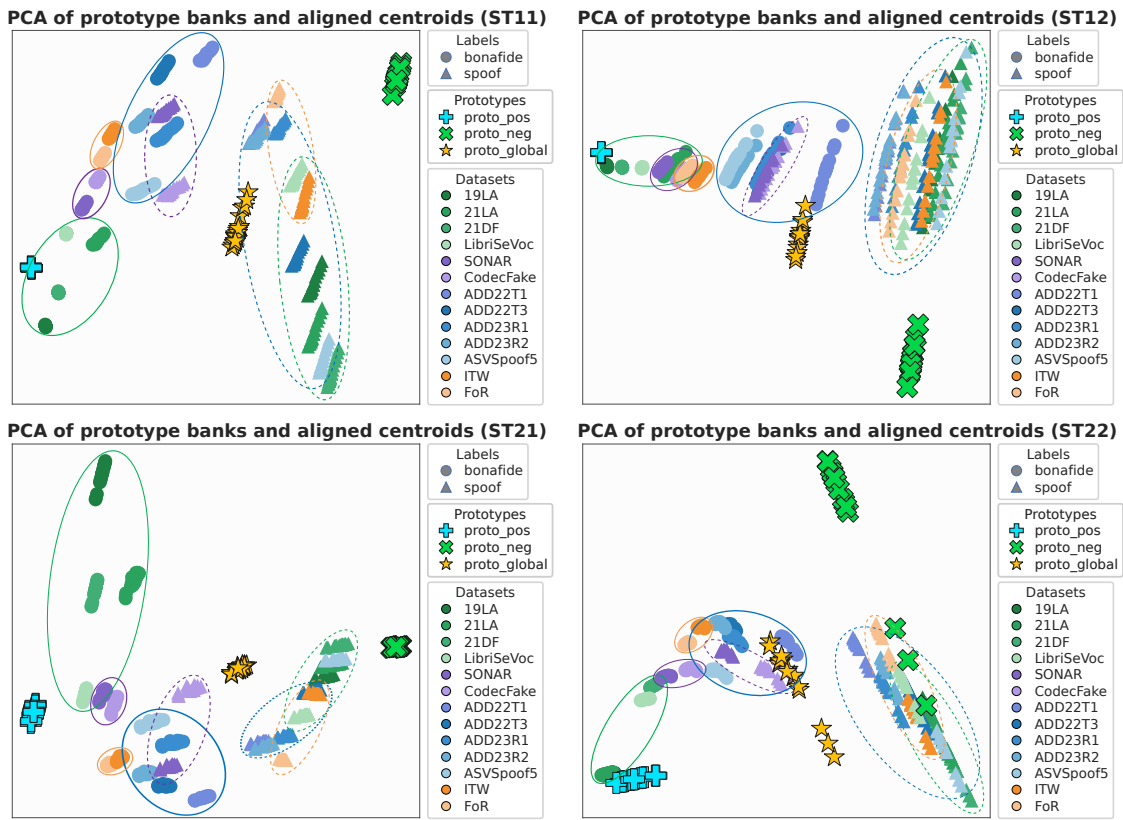


Figure 8: PCA of prototype banks and aligned centroids for four heterogeneous graph layers.